NASA Multi-Frequency Radar for Hydrometeor Phase Identification

Liang Liao (Morgan State Univ.), Robert Meneghini (Goddard Space Flight Center), *Senior Member, IEEE*, Gerald M. Heymsfield (Goddard Space Flight Center), Hyokyung Kim (Morgan State Univ.), and Mei Han (Science Systems & Applications, Inc.)

***Abstract*—This study investigates the potential of dual/multi-frequency Doppler radar for hydrometeor phase classification and develops a phase identification algorithm using NASA airborne radar observations. Theoretical model simulations confirm a clear distinction in both Doppler velocities (V) and dual-frequency Doppler velocities (DDV)—the difference in V at two radar frequencies—between snow and rain hydrometeors. This distinction provides a useful feature for phase identification. A statistical analysis of V and DDV was performed using airborne Doppler measurements from NASA's multi-frequency (X-, Ku-, Ka-, and W-band) radar collected during the IMPACTS field campaign. Results show that snow can be separated from rain using either V or DDV. However, the Linear Depolarization Ratio (LDR) data are required to differentiate snow/rain from mixed-phase (or melting) hydrometeors, as Doppler data alone are insufficient. While the differences in V between snow and rain were found to be larger than in DDV, the air motion independence of DDV is a key advantage. Therefore, a technique leveraging both V and DDV is developed. By combining V, DDV, and LDR, this algorithm successfully classifies hydrometeor phases using the NASA airborne radar dataset.**

***Index Terms*—Dual-/multi-frequency airborne radar, hydrometeor phase identification, Doppler velocity measurements.**

I. INTRODUCTION

Accurate hydrometeor phase knowledge (liquid, frozen, and melting) is crucial for both active/passive remote sensing retrievals of cloud microphysical properties [1]-[3] and for improving climate and weather prediction models [4]. While robust hydrometeor identification methods exist for full-polarimetric radar [5][6], similar techniques are not yet well-established for the non-polarimetric (co-polarization) radars commonly used in airborne and spaceborne weather systems. Accurately identifying phase states from these air/spaceborne systems remains challenging, despite progress in tasks like classifying storm type, determining bright-band height (the altitude where radar reflectivity reaches a local maximum associated with the melting layer), and identifying snow or hail [7]-[9].

Separating liquid and frozen hydrometeors in convective storms, which is essential for studying the rain/snow transition, is particularly difficult with non-polarimetric systems due to the frequent absence of a clearly defined bright band. Previous approaches, such as using combined Ku-band reflectivity and the standard dual-frequency ratio [10][11], perform reasonably well but suffer from significant uncertainties related to attenuation correction, radar calibration, and beam mismatch.

Doppler velocity measurements from dual- and multi-frequency radars offer a promising alternative, leveraging the difference in fall velocities between snow and rain. Crucially, Doppler velocity (V) is independent of radar signal attenuation and insensitive to calibration errors. While V gradients have been used to determine bright-band height [12]-[14], the concept of dual-frequency Doppler velocity (DDV)—the difference in V between two frequencies—is especially useful because it is inherently independent of air motion. Additionally, the Linear Depolarization Ratio (LDR) is an effective tool for identifying mixed-phase hydrometeors, as enhanced LDR signatures are associated with melting particles [15]-[17].

To develop a robust phase identification algorithm for non-polarimetric airborne radar, we explore the potential of multi-frequency Doppler measurements. We first conduct theoretical simulations of V and DDV using frequencies (X-, Ku-, Ka-, and W-band) employed by the NASA/Goddard Space Flight Center (GSFC) airborne radars. Assuming Gamma distributions for snow and rain, these simulations show clear phase separation in V versus mass-weighted diameter (D_m) plots, as well as in DDV versus D_m plots when the frequency separation is large (e.g., X-W, Ku-W, Ka-W). Critically, snow and rain are also distinguishable in the V-DDV plane. To validate these insights and develop a practical algorithm, we utilize actual measurements from the NASA multi-frequency Doppler radar collected during the IMPACTS field campaign [18].

This paper is organized as follows. Section II covers the theoretical background of Doppler velocity and its simulations for snow and rain. Section III describes the NASA multi-frequency Doppler radar measurements. Section IV details the development of the Doppler data-based approaches and provides examples of hydrometeor phases identified using V and DDV, aided by the measured LDR. Concluding remarks are given in Section V.

This work was supported under NASA Investigation of Microphysics and Precipitation for Atlantic Coast-Threatening Snowstorms (IMPACTS) field campaign and Precipitation Measurement Mission (PMM) grants. (Corresponding author: Liang Liao)

Liang Liao and Hyokyung Kim are with Goddard Earth Sciences Technology and Research (GESTAR) II/Morgan State University, Code 612, NASA/GSFC, Greenbelt, MD 20771 USA (e-mail: liang.liao-1@nasa.gov; hyokyung.kim@nasa.gov).

Robert Meneghini and Gerald M. Heymsfield are emeritus with NASA, Code 612, NASA/GSFC, Greenbelt, MD 20771 USA (e-mail: robert.meneghini-1@nasa.gov; gerald.m.heymsfield@nasa.gov).

Mei Han is with Science Systems and Applications Inc, Code 610.1, NASA/GSFC, Greenbelt, MD 20771 USA (e-mail: mei.han-1@nasa.gov).

<

II. Doppler Velocity And Its Simulations

To explore the feasibility of using dual- and multi-frequency Doppler radar for discriminating between snow and rain, we first present the theoretical basis of Doppler velocity and dual-frequency Doppler velocity. We then simulate the distinct Doppler signatures for snow and rain, followed by a discussion of potential techniques for identifying these frozen and liquid phase hydrometeors.

A. Dual-frequency Doppler radar equations

The measured nadir-viewing Doppler velocity (V_m in m/s) at frequency f, is the sum of the reflectivity-weighted mean of the particle fall velocity (V in m/s) and the air motion vector ($\vec{w}$) along the range direction ($\hat{r}$, defined as a unit vector pointing away from radar) [19]-[20] and is given by

$$V_m(f) = (-V(f)\hat{z} + \vec{w}) \cdot \hat{r} \tag{1}$$

where

$$V(f) = \frac{\int_0^\infty N(D)\sigma_b(D,f)V_t(D)dD}{\int_0^\infty N(D)\sigma_b(D,f)dD}, \tag{2}$$

and where $\hat{z}$ is a unit vector along the zenith direction, and $V_t(D)$ (m/s) is the terminal fall velocity of a particle of diameter D in mm. N(D) ($mm^{-1}m^{-3}$) is the particle size distribution and $\sigma_b(D, f)$ is the backscattering cross section of hydrometeor at frequency f. The dual-frequency Doppler velocity (DDV in m/s) is defined as the difference of the measured Doppler velocities at two frequencies and is written as

$$DDV(f_1, f_2) = V_m(f_1) - V_m(f_2) = -[V(f_1) - V(f_2)]\hat{z} \cdot \hat{r}. \tag{3}$$

Snow particle and raindrop size distributions are often expressed in the form of a Gamma distribution:

$$N(D) = N_w f(\mu) \left(\frac{D}{D_m}\right)^\mu \exp(-\Lambda D), \tag{4}$$

where

$$f(\mu) = \frac{6(4+\mu)^{\mu+4}}{4^4\Gamma(\mu+4)}. \tag{5}$$

N_w is the normalized intercept parameter in $mm^{-1}m^{-3}$, and μ is the shape factor of the Gamma distribution. Λ is the slope parameter expressed as

$$\Lambda = {(4+\mu)}/{D_m}, \tag{6}$$

where D_m is the mass-weighted diameter given by

$$D_m = {M_4}/{M_3}, \tag{7}$$

where M_3 and M_4 are the 3rd and 4th moments of N(D), respectively. The i^{th} moment of N(D) is defined by

$$M_i = \int_0^\infty D^i N(D) dD. \tag{8}$$

It should be noted that particle diameter D in above equations and throughout the paper, is referred to as the liquid equivalent diameter, regardless of the hydrometeor phases.

It is not difficult to find from (2)-(4) that V and DDV are a function of D_m and independent of N_w. One of the important features of V and DDV is that it is immune to hydrometeor attenuation as long as the signal-to-noise ratio remains high. This characteristic is particularly important in mixed-phase regions where the attenuation is quite difficult to correct as it depends on the detailed specification of the particle size, shape, and distribution of liquid water within the melting particles. In addition, V and DDV are not sensitive to radar calibration errors. As shown in (3), DDV is not affected by air motion. This invariance is a very useful feature not only from the perspective of deriving the particle size distribution [21]-[24] but also for using this quantity to identify hydrometeor phase in a fast-changing convective system.

B. Simulations of V and DDV in snow and rain

Characterizing the scattering properties of individual snowflakes is extremely challenging due to their highly variable and complex shapes, despite the existence of various scattering models and databases [25]–[27]. For simplicity, but without significant loss of accuracy, we employ a simple scattering model of snow using air-ice mixed spheroids with a constant, size-independent snow density for our simulations. The dielectric constant of the spheroidal air–ice mixture is derived from the Bruggeman mixing formula [28]. While an ice temperature of 0°C is used in the simulations, the dielectric constant of ice varies little with temperature; consequently, the snow scattering results remain nearly unchanged. The validity of this geometric model was previously confirmed by Liao et al. [29], showing reasonably good agreement with scattering results from aggregates (e.g., six-branch bullet-rosettes) when particle masses were preserved. Raindrops are prescribed as oblate spheroids with their aspect ratios following the relations reported by Thurai et al. [30]. For all simulations throughout this paper, the raindrop temperature is set to 15°C. Although varying rain temperatures may affect scattering results more significantly than in the case of snow, the primary goal of these simulations is to demonstrate the fundamental scattering and Doppler properties of both precipitation types. The T-matrix method is used to compute the scattering properties of all single snow and rain particles [31].

Figure 1 displays the computed Doppler velocities (V) as a function of D_m for X-, Ku-, Ka-, and W-bands, assuming a Gamma distribution for N(D) as in (3) with a fixed μ=3. The blue curves represent results for snow with densities ranging from 0.05 to 0.5 g/cm^3, while the red curves represent rain. The terminal velocity of snowflakes in these simulations is based on the results described by Magono and Nakamura [32].

As illustrated in Fig. 1, the V-D_m relations show marked differences between snow and rain, providing a clear basis for phase separation. The primary factor for this separation is the large disparity in fall velocities between snow and rain, while differences in scattering characteristics represent only a secondary effect. Notably, the snow results vary little with snow density. The dynamic ranges of V are much larger for rain than for snow. This suggests that D_m for rain can be inferred from measured V if air motion (which is not included in these simulations) is either known or negligible.

DDV is derived directly from Fig. 1 as the difference between Doppler velocities at two frequencies for a given D_m. Figure 2 exhibits the DDV results for several frequency pairs, with blue

and red curves again corresponding to snow and rain, respectively. Snow DDV generally remains low and close to zero across all pairs. In contrast, the dynamic ranges of rain DDV become appreciable when the W-band is used as one of the two frequencies (e.g., X-W, Ku-W, and Ka-W bands).

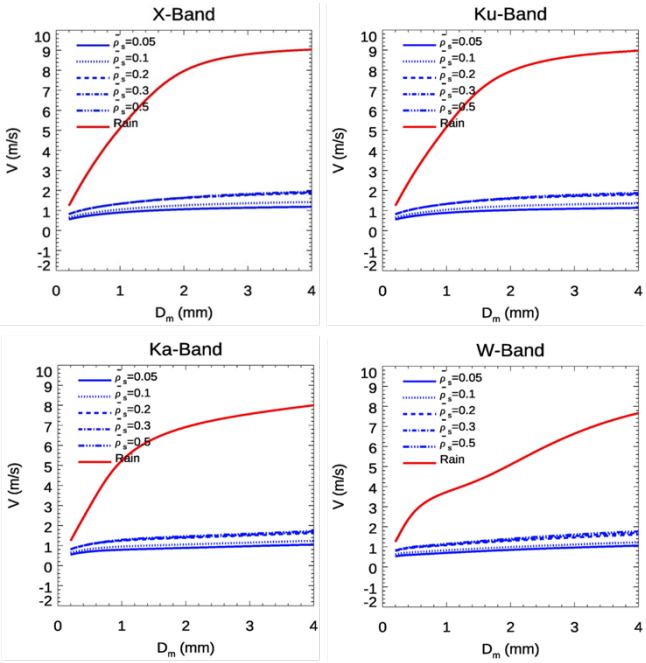


Fig. 1. Theoretical computations of the relationships between Doppler velocity (V) and D_m for snow (blue) and rain (red) at four frequencies, yielding the Gamma distribution for particle and drop size distributions. The snow and rain temperatures are set to 0 and 15 °C, respectively. The snow Doppler velocity computations relied on a simple spheroidal scattering model, assuming the mean snow density ($\bar{\rho}_s$) is independent of particle size. Scattering parameters for rain were computed assuming spheroidal raindrops with aspect ratios based on the shape–size relations reported in [30].

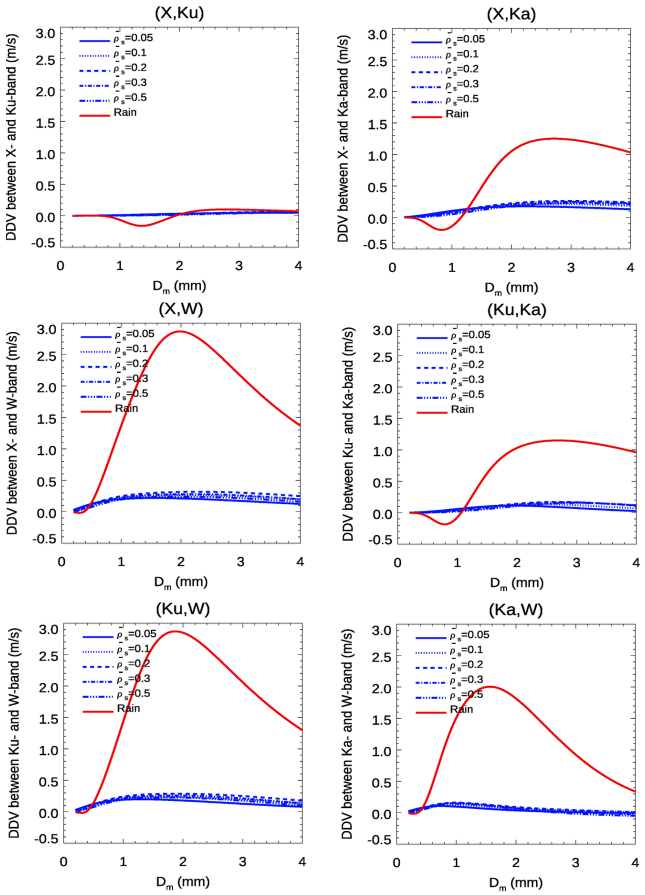


Fig. 2. Theoretical computations of the relationships between DDV and D_m for snow (blue) and rain (red) for various pairs of frequencies, yielding the Gamma distribution for particle and drop size distributions. The snow Doppler velocity computations relied on a simple spheroidal scattering model, assuming the mean snow density ($\bar{\rho}_s$) is independent of particle size. Scattering parameters for rain were computed assuming spheroidal raindrops with aspect ratios based on the shape–size relations reported in [30].

Although the degree of separation in the DDV-D_m plane is not as large as in the V-D_m plane, DDV offers a crucial advantage: it is independent of air motion. Since updraft/downdraft speeds are typically unknown in the atmosphere, this independence makes DDV a superior feature compared to V alone.

Combining DDV and V allows us to leverage both Doppler characteristics for separating snow and rain. Figure 3 illustrates the simulation results in the V-DDV plane. Among the six frequency pairs (X-Ku, X-Ka, X-W, Ku-Ka, Ku-W, and Ka-W), those incorporating the W-band frequency yield the highest DDV values, clearly demonstrating the benefit of using the W-band for effective phase discrimination.

III. NASA Multi-Frequency Airborne Radar Measurements

While theoretical radar simulations are essential for developing and testing new techniques, high-quality radar measurements are required for validation and assessment. For stratiform storms with a well-defined bright band, the simulated Doppler signatures (such as those in Fig. 1–3) can be directly compared with measured Doppler velocities. We will first train phase look-up tables—which classify hydrometeor phase using radar Doppler inputs—with measurements of snow, mixed-phase, and rain taken under stratiform conditions, and then apply these tables to other storm types.

NASA/GSFC utilizes three complementary airborne radar systems: the High-altitude Imaging Wind and Rain Airborne Profiler (HIWRAP) operating at Ku- and Ka-band, the Cloud Radar System (CRS) at W-band, and the ER-2 X-band Radar (EXRAD) [33]-[36]. The specifications for these systems are detailed in Table I. Figure 4 illustrates the NASA ER-2 payload during the IMPACTS (Investigation of Microphysics and Precipitation for Atlantic Coast – Threatening Snowstorms) field campaign in 2020, 2022, and 2023. This combination of CRS, HIWRAP, and EXRAD provides four-frequency (X-, Ku-

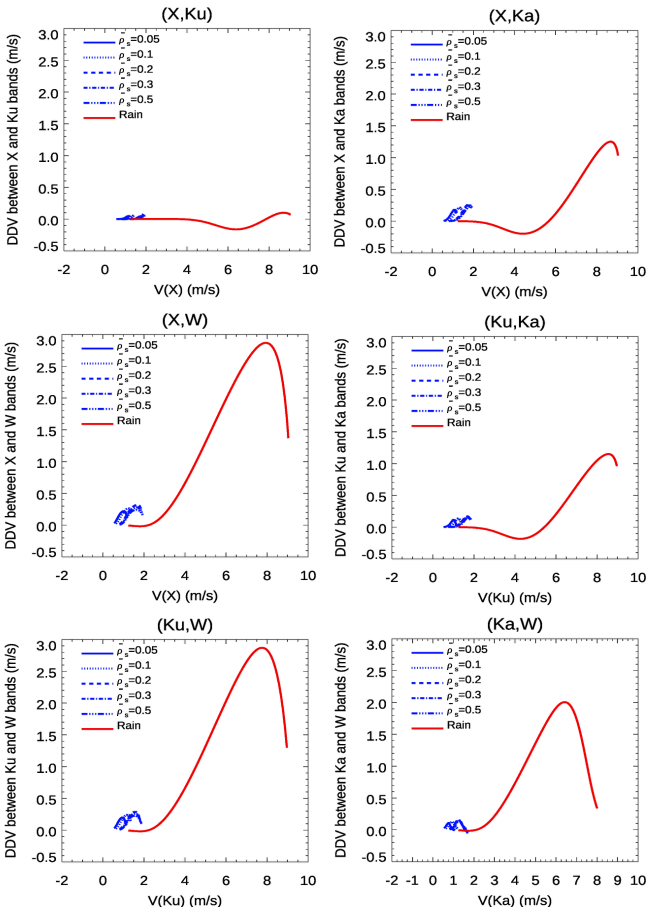


Fig. 3. Theoretical computations of the relationships between DDV and V for snow (blue) and rain (red) for various pairs of frequencies, yielding the Gamma distribution for particle and drop size distributions. The snow Doppler velocity computations relied on a simple spheroidal scattering model, assuming the mean snow density ($\bar{\rho}_s$) is independent of particle size. Scattering parameters for rain were computed assuming spheroidal raindrops with aspect ratios based on the shape–size relations reported in [30].

, Ka-, W-band) reflectivity and Doppler measurements from precipitation and clouds, including Linear Depolarization Ratio (LDR) measurements at Ku-, Ka-, and W-band. *NASA ER-2* Doppler radars compensate for aircraft motion by integrating precise measurements of aircraft velocity and attitude. By subtracting the motion-induced Doppler shift from raw measurements, only the atmospheric Doppler velocity remains. The efficacy of this correction is evaluated using surface returns, where the mean Doppler velocity should ideally be zero. Resulting biases and standard deviations are instrument-dependent and are summarized in Table II. IMPACTS data collection including HIWRAP can be obtained from the Global Hydrology Resource Center Distributed Active Archive Center at http://dx.doi.org/10.5067/IMPACTS/DATA101. Additional information can be found in [37].

Figure 5 illustrates an example of the multi-frequency radar measurements—reflectivity (left column), Doppler velocity (middle column), and LDR (right column)—collected over a 200-km segment of the storm on February 17, 2022, primarily covering central and southern Indiana, as well as southwestern Ohio and parts of northern Kentucky, during the IMPACTS campaign. The flight path is shown in the bottom panel, with longitude (red horizontal), latitude (red vertical), and relative flight distance (black) indicated.

The four-frequency reflectivity measurements clearly capture the storm's detailed structure, though the X-band reflectivities show a positive offset relative to the Ku-band, likely due to a radar calibration issue. While calibration offsets generally do not affect Doppler velocity measurements, aircraft motions (pitch, yaw, and roll) must be accounted for.

TABLE I
SPECIFICATIONS OF NASA HIGH ALTITUDE AIRBORNE RADAR

	CRS	HIWRAP	EXRAD
Frequency (GHz)	94.00 (W-band)	13.91 (Ku-band) 35.56 (Ka-band)	9.60 (X-band)
Transmitter	SSPA	SSPA	TWT
RF Peak Power (W)	30	80 Ku/ 40 Ka	9000
Measurements	Ref, Dopp, LDR, Spec Wid	Ref, Dopp, LDR, Spec Wid	Ref, Dopp, Spec Wid
Antenna Beam Width (deg)	0.46	3.0 Ku/ 1.2 Ka	3.3
Vertical Resolution (m)	115	145	110
Vertical Sampling (m)	26.25	26.25	18.74
Horizontal Resolution at Surface (m)	160	1050 (Ku), 420 (Ka)	1150
Horizontal Sampling (m)	50	100	50
Beam Pointing	Nadir	Conical scan (GH, WB57) Nadir (ER-2)	Nadir & conical scan
Approximate Minimum Detectable Reflectivity (dBZe @10 km range)	-28	-13	-13 Nadir/ -8 Scanning
Doppler Nyquist Range (m/s)	14.2	96.2 Ku/ 37.9 Ka	156.2

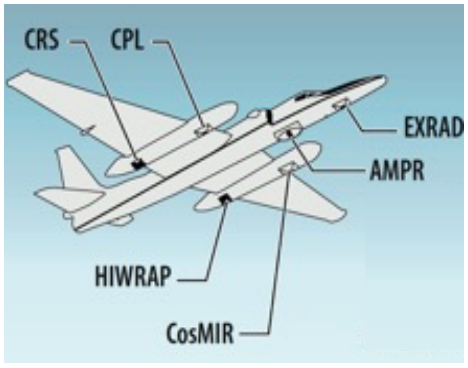


Fig. 4. NASA ER-2 radar payload: HIWRAP, CRS and EXRAD. Also mounted in the ER-2 aircraft are Cloud Physics Lidar (CPL) for observing vertical structure of clouds and aerosols, Advanced Microwave Precipitation Radiometer (AMPR) for measuring precipitation structure and intensity.

TABLE II
MEASUREMENT BIAS (M/S) AND STANDARD DEVIATION (STD, M/S) OF NASA ER-2 RADAR AT X, KU, KA AND W BANDS

	X	Ku	Ka	W
Bias	-0.355165	0.377526	-0.203125	0.132612
STD	0.828807	0.917864	0.367628	0.250418

The LDR data provide an excellent indicator of the mixed-phase region (melting snow) [15][17]. This is a result of

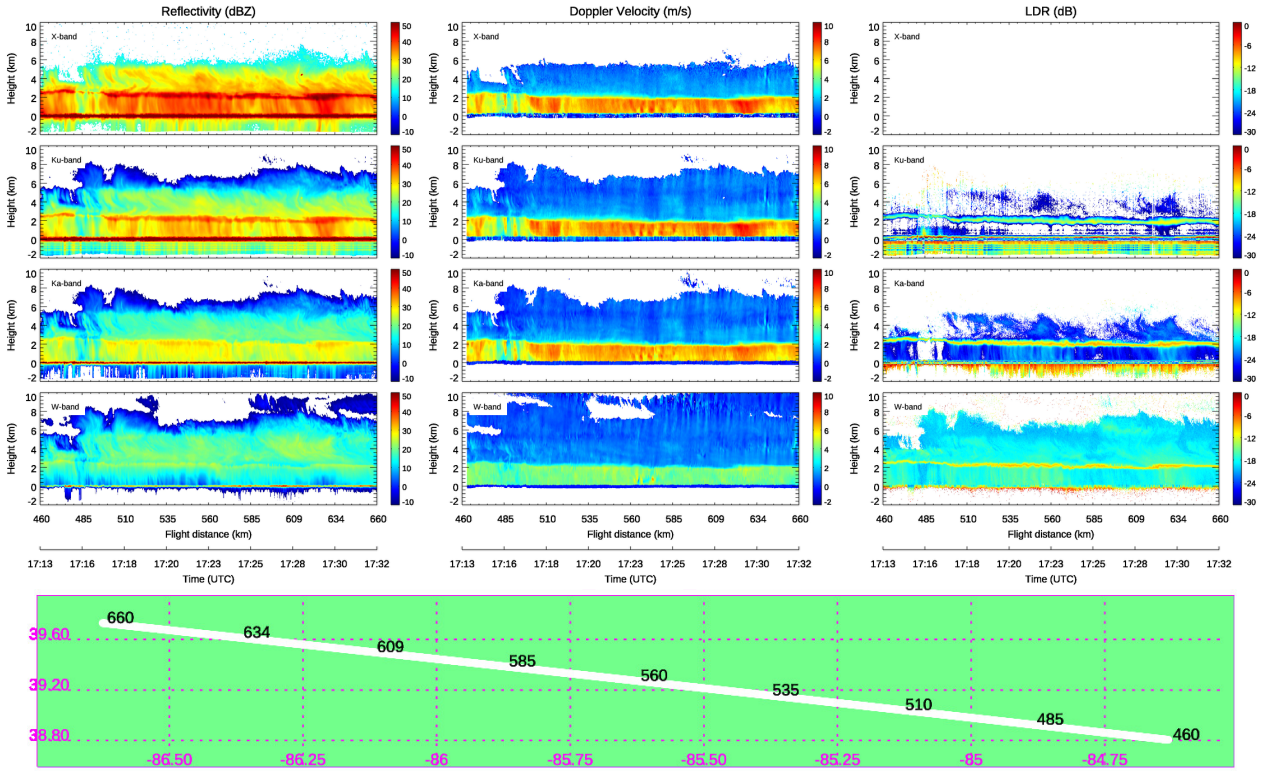


Fig. 5. Measurements from the NASA ER-2 Radar during IMPACTS on 17 February 2022. The panels display, from left to right: the radar reflectivity factor, Doppler velocity, and LDR. Data are shown for the X-band (top row), Ku-band (second row), Ka-band (third row), and W-band (bottom row). The lower panel shows the ER-2 flight track (heavy white line) corresponding to these measurements. Flight distance, relative to the recording start, is given by black numbers along the track. Red numbers on the horizontal and vertical axes indicate longitude and latitude, respectively. Green shading indicates land.

enhanced reflectivity from non-spherical melting snowflakes, a phenomenon previously documented in other airborne radar campaigns [38]. As seen in Fig. 5, a strong LDR band is clearly visible at Ku-, Ka-, and W-bands around 2 km height, which corresponds to the melting layer or bright band commonly found in stratiform storms. Note that due to the minimum detectable signal limitation, LDR cannot always be detected in light rain where the cross-polar received power often falls below the radar noise floor.

Achieving precise and accurate Doppler data from the fast-moving NASA high-altitude aircraft requires several complex correction procedures. These include removing apparent Doppler signatures caused by the aircraft's high speed, correcting for non-uniform beam filling (NUBF) effects, and unfolding measured Doppler velocities that exceed the Nyquist velocity. These critical processing steps are fully documented in [39].

IV. Hydrometeor Phase Identification Methods

As shown in Fig. 5, the LDR measurements exhibit noise across all three frequencies (Ku-, Ka-, and W-bands), with Ku-band LDR appearing the noisiest and Ka-band LDR showing the highest quality. The less-noisy Ka-band LDR within the melting layer provides a reliable indication of mixed-phase particles. To mitigate the observed noise and improve overall detectability, the LDR approach for mixed-phase identification employs measurements from all three frequencies, as illustrated in Fig. 6. The frequency-dependent LDR thresholds were derived by analyzing the noise levels and the strength of LDR signals within the melting region using data collected during the IMPACTS campaign.

After applying the LDR mixed-phase detection procedures (illustrated in Fig. 6) to the stratiform precipitation data from

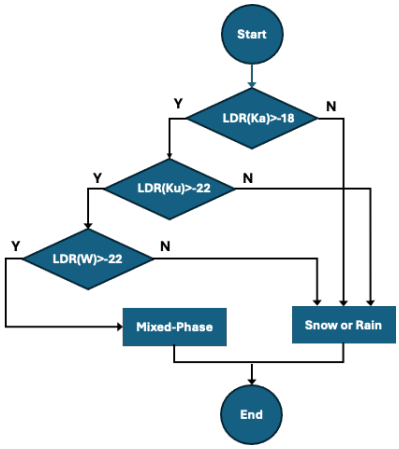


Fig. 6. Procedures for identification of mixed-phase hydrometeors with use of LDR signatures.

the entire February 17, 2022, flight (~5000 km), the measured Doppler velocities were categorized into snow, mixed-phase, and rain datasets. Figure 7 presents the probability density functions (PDFs) of these measured Doppler velocities for each frequency: X-band (top-left), Ku-band (top-right), Ka-band (bottom-left), and W-band (bottom-right). The solid, dotted, and dashed lines represent snow, rain, and mixed particles, respectively.

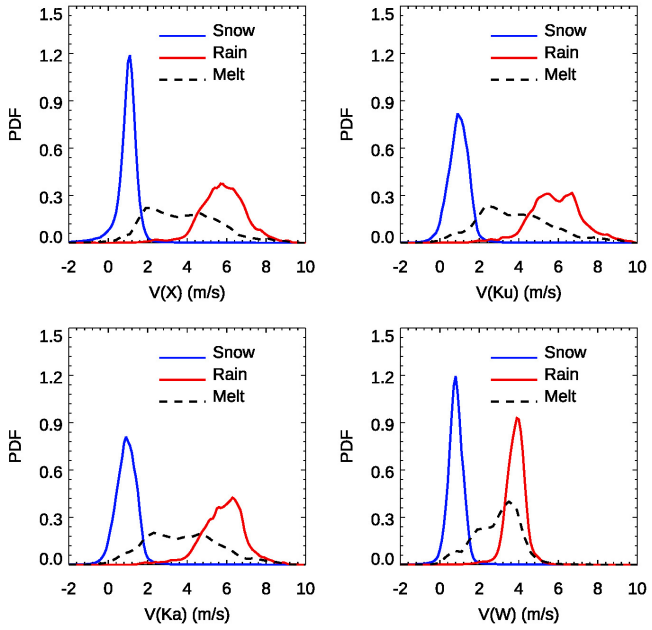


Fig. 7. Doppler Velocity PDFs for snow, rain, and mixed-phase hydrometeors (17 February 2022). These plots present the Probability Density Functions of Doppler velocities measured in stratiform precipitation using the entire flight data. Frequencies are shown across four panels: X-band (top-left), Ku-band (top-right), Ka-band (bottom-left), and W-band (bottom-right). Hydrometeor phases, classified using LDR signatures, are represented by solid lines (snow), dotted lines (rain), and dashed lines (mixed-phase).

Across all frequencies, there is a clear separation between the PDFs of snow and rain in terms of the magnitude of the Doppler velocity. Snow velocities primarily reside in the 0–2 m/s range, while rain velocities occupy a range of relatively larger magnitudes. This separation is wider at the X-, Ku-, and Ka-bands than at the W-band, a distinction attributable to substantial differences in radar backscattering cross-sections between the frequency groups. These results are obtained directly from the measurements, which include air motion (though minimal for stratiform cases). Importantly, the Doppler velocities of mixed-phase (melting snow) are distributed across the entire range of both snow and rain, demonstrating that mixed-phase hydrometeors are nearly indistinguishable from snow and rain based on the Doppler velocity magnitude alone.

The PDFs of DDV shown in Fig. 8 for the X-W (top-left), Ku-Ka (top-right), Ku-W (bottom-left), and Ka-W (bottom-right) pairs are statistically similar to the single-frequency Doppler velocity PDFs presented in Fig. 7. As expected, mixed-phase hydrometeors cannot be separated from either snow or rain using DDV alone. However, most snow data are distinguishable from rain for the frequency pairs involving the W-band (X-W, Ku-W, and Ka-W). The small overlap of rain data with the snow PDF is primarily attributed to mismatched measurements between radar frequencies. Separation of snow from rain is difficult for the Ku-Ka pair because the rain DDV is not sufficiently large relative to the snow DDV for effective discrimination.

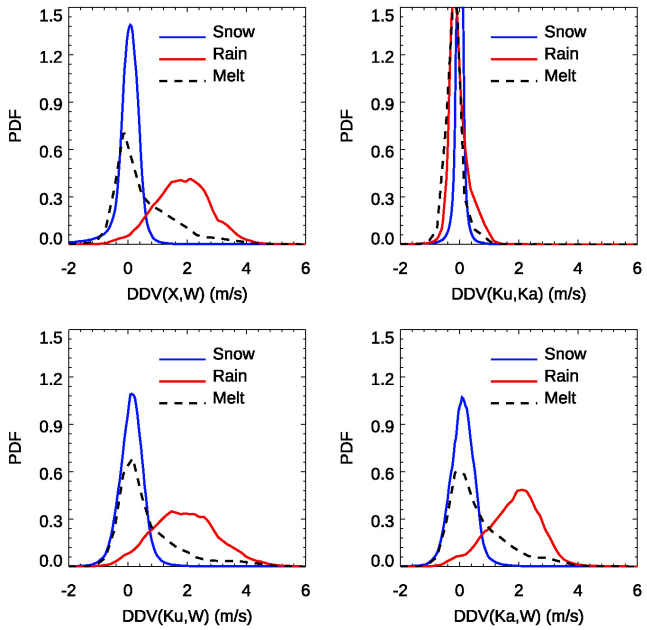


Fig. 8. PDFs of DDV on 17 February 2022. The panels show DDV PDFs derived from stratiform precipitation during the entire flight, calculated using four frequency pairs: X- and W-band (top-left), Ku- and Ka-band (top-right), Ku- and W-band (bottom-left), and Ka- and W-band (bottom-right). Hydrometeors are classified by LDR signatures (as detailed in Fig. 5) into snow (solid lines), rain (dotted lines), and mixed-phase (dashed lines).

To leverage the strengths of both parameters—DDV's independence from air motion and V's larger snow-rain separation—we exploit their joint distributions (two-dimensional PDFs). Using the same data presented in Figs. 7 and 8, the two-dimensional PDFs of DDV and V are plotted in Fig. 9 for the four frequency pairs from Fig. 8. In the DDV-V plane, two completely separated data clusters are clearly visible: the small, focused clusters are associated with snow, and the elongated areas correspond to rain particles. Comparing the measured DDV and V in Fig. 10 with the theoretical simulations in Fig. 3 shows a strong consistency. However, the measured DDV exhibits slightly larger negative values than predicted by the model. These negative values are likely artifacts of measurement noise, uncertainties in the Doppler aircraft-motion correction, and radar beam mismatches between the two frequencies.

Figure 10 offers an alternative visualization of the data

distributions using PDF contours that enclose the data populations at the 40% (red), 70% (yellow), and 90% (cyan) levels. Two distinct clusters, labeled 'Snow' and 'Rain', clearly represent the respective particle populations. Quantitative analysis reveals that more than 90% of the snow and rain data are separable in the DDV-V plane when using the X-W, Ku-W, and Ka-W frequency pairs.

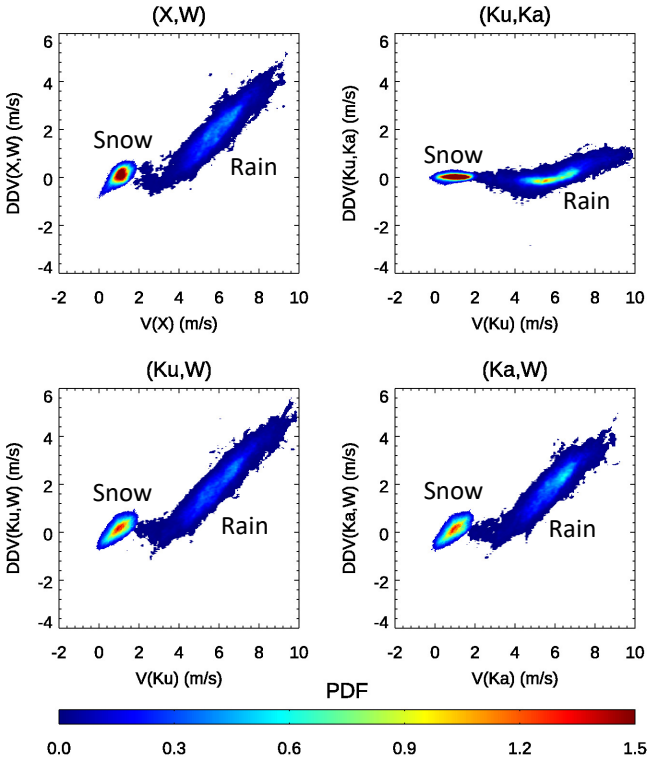


Fig. 9. Density scatter plots (2D PDFs) of DDV vs. V. These plots are derived from the data presented in Figs.7 and 8. The four panels show the following relationships: Top-left: DDV(X,W) vs. V(X); Top-right: DDV(Ku,Ka) vs. V(Ku); Bottom-left: DDV(Ku,W) vs. V(Ku); Bottom-right: DDV(Ka,W) vs. V(Ka).

Figures 9 and 10 clearly demonstrate that the combination of DDV and V provides an effective way to discriminate between snow and rain particles. To develop a practical classification algorithm, we require phase look-up tables that link DDV and V to specific phase states for each frequency pair.

The frequency pairs incorporating the W-band (X-W, Ku-W, and Ka-W) produce relatively large rain DDV values, resulting in the best separation from the snow distribution. In contrast, combinations that exclude the W-band (X-Ku, X-Ka, and Ku-Ka) do not yield clear separation. For this reason, our classification approach focuses primarily on the X-W, Ku-W, and Ka-W frequency pairs.

Figure 11 provides an example of the look-up table constructed in the DDV-V plane for the Ka- and W-band pair, derived from the results in Figs.9 and 10. The regions colored blue correspond to snow, and the areas in red correspond to rain. Specifically, hydrometeors are classified as snow if their measured DDV and V fall within the blue region, and as rain if they fall within the red area. Similar phase look-up tables have been constructed for the other optimal frequency pairs (not shown).

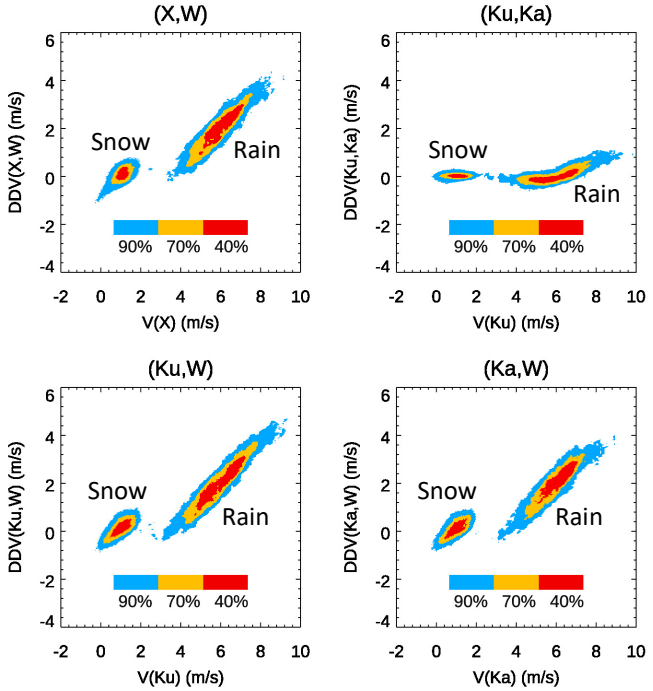


Fig. 10. Density scatter plots of DDV vs. V, similar to Fig. 9, but with PDF contours. The contours enclose the data population at levels of 40% (red), 70% (yellow), and 90% (cyan). The two distinct clusters are labeled 'Snow' and 'Rain', representing their respective hydrometeor populations.

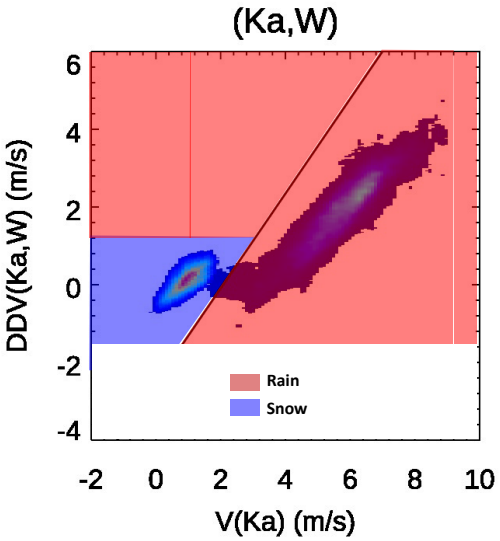


Fig. 11. Schematic classification of snow and rain using DDV and V. This diagram shows how DDV and V measurements are used to classify hydrometeors. The blue area denotes the defined region for snow occurrence, and the red area denotes the region associated with rain. This classification utilizes the combined Doppler measurements from the Ka- and W-bands.

It is important to note that the phase look-up tables based on

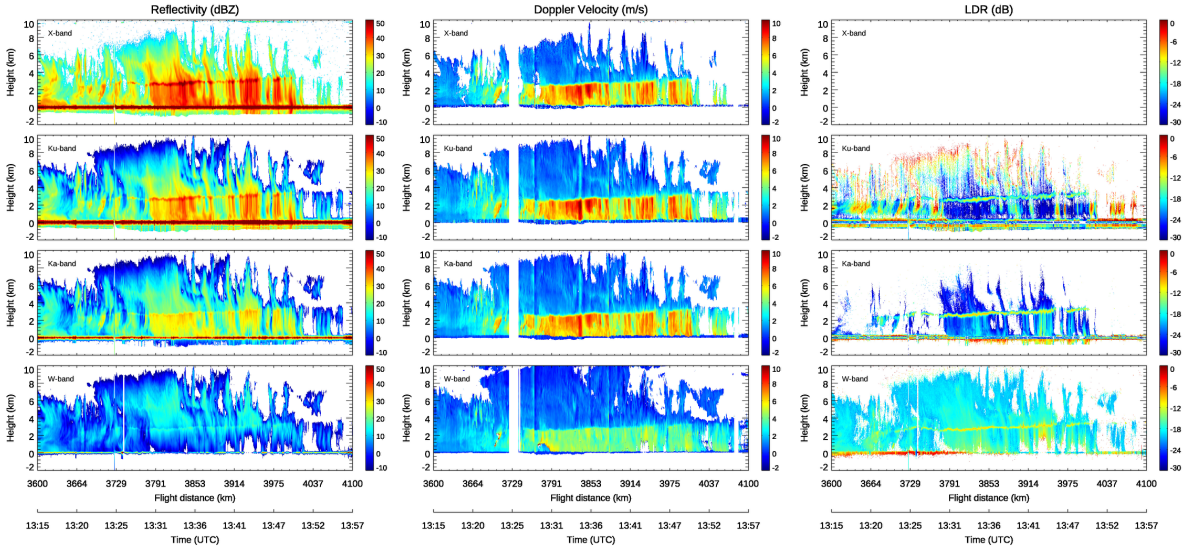


Fig. 12. Measurements from the NASA ER-2 radar during IMPACTS on 25 February 2022. The panels are organized by frequency band: X (top row), Ku (second row), Ka (third row), and W (bottom row). The columns display the radar reflectivity factor (left), Doppler velocity (middle), and LDR (right) for each band.

DDV and V, as illustrated in Fig. 11, are only used to separate snow and rain. They are not applicable for distinguishing mixed-phase particles from snow and rain, as the DDV and V data for mixed-phase hydrometeors are broadly distributed across the snow and rain regions (as shown in Figs. 7 and 8). The mixed-phase particles, however, are effectively detected using the LDR data, as established in Fig. 6.

The phase look-up tables can be expressed mathematically. The measurements are classified as snow if their DDV and V satisfy:

$$1.3 \geq DDV \geq aV + b, \tag{9}$$

where a and b are constants that are functions of the chosen frequency pairs, with their values detailed in Table II. Data points that do not satisfy this condition are classified as rain. It must be noted that the look-up tables described by (9) and Table III are applicable exclusively to the NASA ER-2 airborne radar deployed during IMPACTS. This specificity arises because the table values are inherently affected by measurement uncertainties, including beam mismatches, errors from aircraft motion correction, and the number of independent samples used for data averaging. Future work utilizing closely beam-matched data is expected to significantly reduce data variability, which would lead to improved snow and rain separation.

TABLE III
DEPENDENCE OF PARAMETERS a AND b IN (9) ON RADAR FREQUENCY PAIRS

	a	b
X-W	1.2987	-2.9610
Ku-W	1.3889	-3.1667
Ka-W	1.2195	-2.5366

The procedure for classifying the NASA multi-frequency Doppler radar measurements into snow, rain and mixed-phase regions comprises two steps: First, mixed-phase regions are identified using LDR signatures (Fig. 6). Second, snow and rain are classified from the non-mixed-phase data using the DDV-V phase look-up tables.

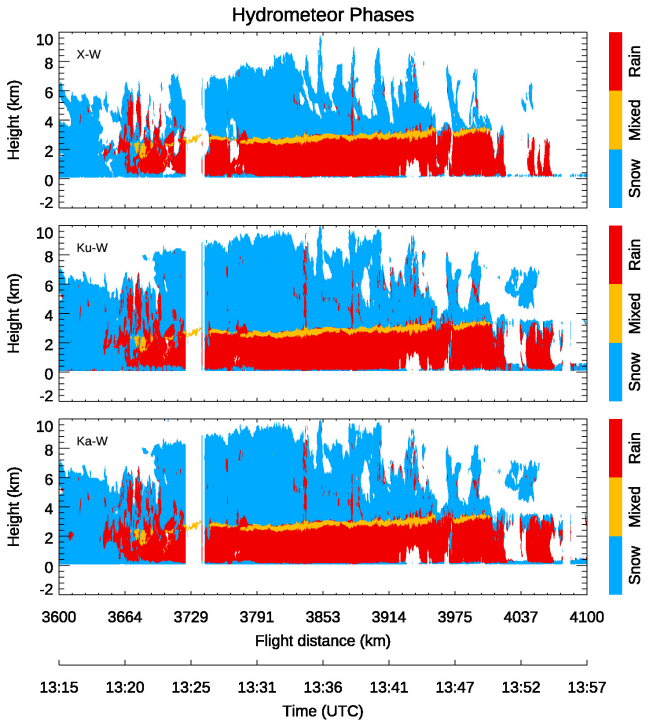


Fig. 13. Hydrometeor phase state classification using dual-frequency combinations. The panels show the hydrometeor phase states identified for the measurement segment presented in Fig. 12, based on the following radar frequency pairs: X-W bands (top panel), Ku-W bands (middle panel), and Ka-W bands (bottom panel). The colors represent: snow (blue), rain (yellow), and mixed-phase (red) hydrometeors.

To test this algorithm, we applied it to NASA's four-frequency Doppler measurements collected on February 25, 2022, during IMPACTS, which are displayed in Fig. 12. We note that because of inherent difficulties with aircraft motion correction, Doppler data are sometimes unreliable; these unreliable points are excluded from the classification (e.g., the gap near the 3729 km distance mark where the aircraft was banking).

The classified hydrometeor phases are shown in Fig. 13 for the three optimal frequency pairs: X-W (top), Ku-W (middle), and Ka-W (bottom). Despite minor differences among the results—caused mainly by varying sensitivities of the individual radars—the identified hydrometeor phases are generally very consistent, confirming that each of these W-band-inclusive frequency pairs performs reasonably well.

The classification results reflect physically and logically reasonable storm structures consistent with the radar reflectivity measurements in Fig. 12. From 13:15 to 13:20 UTC, the storm is primarily composed of snow. During the 13:20–13:25 UTC period, we observe notable convective features and the absence of a bright-band. The classification of some particles as rain above the 2 km freezing level may be associated with convective updraft/downdraft processes. Alternatively, these could be mixed-phase particles where the cross-polarized LDR signal was too weak for detection. Further verification requires additional, independent observations, which we designate as future work. Observations recorded after 13:25 UTC show typical stratiform precipitation with a clearly defined bright-band, indicating the melting layer that separates snow from rain. The phases identified in Fig. 13 based on Doppler and LDR measurements are thus highly consistent with the storm's overall structural evolution. In certain regions (notably after 13:25 UTC), snow is occasionally misclassified as rain. This is likely attributable to errors in the aircraft motion correction applied to the Doppler measurements. Spatial smoothing and filtering procedures are expected to remove these isolated, discontinuous clusters that differ from their surrounding phase, thereby improving the overall classification. Furthermore, fine-tuning the phase look-up tables is expected to further enhance the results.

Classification accuracy can be evaluated most reliably in stratiform regions where snow and rain are clearly separated by a well-defined melting layer (bright band). For the stratiform case shown in Fig. 13, the snow classification accuracy rates are 94%, 92%, and 92% for the X-W, Ku-W, and Ka-W band frequency pairs, respectively. Similarly, the corresponding accuracy rates for rain are 96%, 96%, and 97%. Due to the lack of truth for hydrometeor phases within convective cores, a quantitative assessment of classification accuracy is not performed for those regions.

V. Remarks

The primary goal of this study is to assess the feasibility of dual-/multi-frequency Doppler radar for hydrometeor phase classification and to develop a corresponding algorithm for the NASA multi-frequency Doppler radar. While theoretical simulations show large differences in Doppler velocity between snow and rain—a useful classification feature—V alone is inadequate because it is susceptible to air motion, which hinders accurate separation in convective storms. To overcome this, we incorporate the dual-frequency Doppler velocity, which is inherently independent of air motion. Theoretical studies confirm that DDV values for snow and rain are distinguishable provided the frequency separation is sufficiently large (e.g., X-W, Ku-W, and Ka-W bands). By combining V and DDV, we leverage the benefits of both. A significant advantage is that both V and DDV are immune to attenuation (from precipitation, cloud, vapor, and oxygen) and insensitive to radar calibration offsets—crucial benefits, especially given the challenges of attenuation correction at high frequencies like Ka- and W-bands.

To develop and test the Doppler velocity-based phase identification algorithm, we utilized Doppler data from the NASA multi-frequency airborne radar during the IMPACTS field campaign. We derived the density distributions (PDFs) of V and DDV separately for snow, mixed-phase, and rain using data from stratiform precipitation events, where the melting layer (and phase separation) was determined by LDR signatures. The joint distributions of V and DDV for snow and rain exhibit clear separation, and the achieved statistical distributions are generally consistent with theoretical model computations. The resulting V-DDV phase look-up tables, constructed directly from these measurements, are designed only to separate snow and rain. Distinguishing mixed-phase hydrometeors from snow and rain requires the complementary LDR measurements.

The developed phase identification algorithm was successfully applied to the NASA airborne Doppler measurements. The phases identified across the three optimal frequency pairs (X-W, Ku-W, and Ka-W bands) were found to be consistent and the results reasonable. Snow and rain detection does not depend on the presence of a bright band, meaning the algorithm can, in principle, be applied effectively to convective storms where a bright band is absent. However, the Doppler measurements are susceptible to uncertainties associated with uncorrected aircraft motion effects. The effectiveness of the aircraft motion correction can be assessed by checking that the Doppler velocities at the surface are close to zero. It is worth noting that hydrometeor phases can be independently derived using a reflectivity-based approach involving Ku-band reflectivity and the Ku/Ka-band dual-frequency ratio (DFR) [10][11]. This method, however, demands high-quality radar measurements, including accurate calibration, beam-matched data, and meticulous attenuation correction. Due to the differences in antenna beam widths among the NASA airborne radar frequencies, the noise level of the DFR measurements often exceeds the threshold required for reliable classification in cases of light rain and snow. Compared to the reflectivity-based approach for NASA airborne measurements, Doppler-based techniques are more robust and effective, despite current limitations stemming from unmatched-beam measurements. Further studies will include

refinement of the phase look-up tables and validation of the results using independent measurements and estimates, such as comparisons with fully-polarimetric ground radar measurements.

ACKNOWLEDGEMENT

The authors are appreciative of the IMPACTS science and instrument teams for their excellent data collection used in this study.

REFERENCES

[1] S. Seto, T. Iguchi, R. Meneghini, J. Awaka, T. Kubota, T. Masaki, and N. Takahashi, "The Precipitation Rate Retrieval Algorithms for the GPM Dual-frequency Precipitation Radar," *J. Meteorol. Soc. Jpn.*, vol. 99, pp. 205–237, 2021.

[2] L. Liao and R. Meneghini, 2022: GPM DPR retrievals: algorithm, evaluation, and validation. *Remote Sens*., vol. 14, pp. 843, 2022, https://doi.org/10.3390/rs14040843.

[3] M. Grecu, W. S. Olson, S. J. Munchak, S. Ringerud, L. Liao, Z. Haddad, B. L. Kelley, and S. F. McLaughlin, "The GPM combined algorithm," *J. Atmos. Oceanic Technol*., vol. 33, pp. 2225-2245, 2016.

[4] W.-K. Tao et al., "*Microphysics in Goddard multi-scale modeling systems: A review, in Current trends in the representation of physical processes in weather and climate models*," Springer, pp. 253-316, 2019.

[5] A. V. Ryzhkov, T. J. Schuur, D. W. Burgess, P. L. Heinselman, S. E. Giangrande, and D. S. Zrnić, "The Joint Polarization Experiment: Polarimetric rainfall measurements and hydrometeor classification," *Bull. Amer. Meteor. Soc.*, vol. 86, pp. 809–824, 2005.

[6] H. S. Park, A.V. Ryzhkov, D.S. Zrnić, and K. Kim, "The Hydrometeor Classification Algorithm for the Polarimetric WSR-88D: Description and Application to an MCS," *Wea. Forecasting,* vol. 24, pp. 730–748, 2009.

[7] J. Awaka, M. Le, S. Brodzik, T. Kubota, T. Masaki, V. Chandrasekar, and T. Iguchi, "Improvements of rain type classification algorithms for a full scan mode of GPM Dual-frequency Precipitation Radar," *J. Meteor. Soc. Jpn*., vol. 99, pp. 1253–1270, 2021.

[8] M. Le and V. Chandrasekar, "Hydrometeor profile characterization method for dual-frequency precipitation radar onboard the GPM," *IEEE Trans. Geosci. Remote Sens.*, vol. 51, pp. 3648-3658, 2013.

[9] M. Le and V. Chandrasekar, "Graupel and hail identification algorithm for the Dual-Frequency Precipitation Radar (DPR) on the GPM core satellite," *J. Meteor. Soc. Japan*, vol. 99, pp. 49-65, 2021.

[10] L. Liao and R. Meneghini, "A Study on the feasibility of dual-wavelength radar for identification of hydrometeor phases," *J. Appl. Meteorol. Climatol.*, vol. 50, pp. 449-456, 2011.

[11] L. Liao and R. Meneghini, "A dual-wavelength radar technique to detect hydrometeor phases," *IEEE Geosci. Remote Sens*, vol. 54, pp. 7292-7298, 2016.

[12] T. Pfaff, A. Engelbrecht, and J. Seidel, "Detection of the bright band with a vertically pointing k-band radar," *Meteor. Z.*, vol. 23, pp. 527–534, 2014, https://doi.org/10.1127/metz/2014/0605.

[13] D. Lin, B. Pickering, and R. R. Neely III, "Relating the Radar Bright Band and Its Strength to Surface Rainfall Rate Using an Automated Approach," *J. Hydrometeor*., vol. 21, pp. 335–353, 2020, https://doi.org/10.1175/JHM-D-19-0085.1.

[14] J. A. Shates, C. Pettersen, T. S. L'Ecuyer, and M. S. Kulie, "Multi-year analysis of rain-snow levels at Marquette, Michigan," *Journal of Geophysical Research: Atmospheres*, vol. 128, 2023.

[15] H. Liu and V. Chandrasekar, 2000: Classification of hydrometeors based on polarimetric radar measurements: Development of fuzzy logic and neuro-fuzzy systems, and in situ verification. *J. Atmos. Ocean. Technol*., vol. 17, pp. 140-164, 2000.

[16] S. Tanelli, J. P. Meagher, S. L. Durden, and E. Im, "Processing of high resolution, multiparametric radar data for the airborne dual-frequency precipitation radar APR-2." in *Proc. 4th SPIE Int. Asia-Pacific Symp. Remote Sens*., Honolulu, HI, USA, pp. 25–32, 2004.

[17] R. Bechini and V. Chandrasekar, "A semisupervised robust hydrometeor classification method for dual-polarization radar applications," *J. Atmos. Ocean. Technol.*, vol. 32, 22–47, 2015.

[18] L. A. McMurdie et al., "Chasing snowstorms: The Investigation of Microphysics and Precipitation for Atlantic Coast-Threatening Snowstorms (IMPACTS) campaign," *Bull. Amer. Meteor. Soc*., vol. 103, E1243–E1269, 2022, https://doi.org/10.1175/BAMS-D-20-0246.1.

[19] J. Doviak and D. S. Zrnić, *Doppler Radar and Weather Observations*, 2nd ed. Cambridge, MA, USA: Academic Press, 1993.

[20] V. N. Bringi and V. Chandrasekar, *Polarimetric Doppler Weather Radar: Principles and Applications*. Cambridge, U.K.: Cambridge Univ. Press, 2001.

[21] R. Meneghini, L. Liao, S. W. Bidwell, and G. M. Heymsfield, "On the feasibility of a Doppler weather radar for estimates of drop size distribution using two closely-spaced frequencies," *IEEE Trans. Geosci. Remote Sens*., vol. 39, pp. 2203–2216, 2001.

[22] R. Meneghini, S. W. Bidwell, R. Rincon, G. M. Heymsfield, and L. Liao, "Differential-frequency Doppler weather radar: Theory and experiment," *Radio Sci*., vol. 38, pp. 8040, 2003, doi:10.1029/2002RS002656.

[23] L. Tian, G. M. Heymsfield, L. Li, and R. Srivastava, "Properties of light stratiform rain derived from 10 and 94 GHz airborne Doppler radars," *J. Geophys. Res*., vol. 112, D11 211, 2007.

[24] L. Liao, R. Meneghini, L. Tian, and G. Heymsfield, "Retrieval of snow and rain from combined X- and W-band airborne radar measurements," *IEEE Geosci. Remote Sens*., vol. 46, pp. 1514-1524, 2008.

[25] G. Liu, "A database of microwave single-scattering properties for non-spherical ice particles," *Bull. Am. Meteorol. Soc*., vol. 89, pp. 1563-1570, 2008.

[26] H. Nowell, G. Liu, and R. Honeyager, "Modeling the microwave single-scattering properties of aggregate snowflakes.," *J. Geophys. Res. Atmos*., vol. 118, pp. 7873–7885, 2013, doi:10.1002/jgrd.50620.

[27] K-S Kuo, W. S. Olson, B. T. Johnson, M. Grecu, L. Tian, T. L. Clune, B. H. van Aartsen, A. J. Heymsfield, L. Liao, and R. Meneghini, "The microwave radiative properties of falling snow derived from realistic ice particle models. Part I: An extensive database of simulated pristine crystals and aggregate particles, and their scattering properties," *J. Appl. Meteorol. Climatol*., vol. 55, pp. 691-708, 2015.

[28] D. A. G. Bruggeman, "Berechnung verschiedener physikalischer Konstanten von heterogenen Substanzen. I. Dielektrizitätskonstanten und Leitfähigkeiten der Mischkörper aus isotropen Substanzen," *Ann. Phys.*, vol. 416, no. 7, pp. 636–649, 1935.

[29] L. Liao, R. Meneghini, H. Nowell and G. Liu, "Scattering computations of snow aggregates from simple geometrical particle models," *IEEE J. Selected Topics in Earth Obs. and Remote Sens*., vol. 6, pp. 1409-1417, 2013.

[30] M. Thurai, G. J. Huang, V. N. Bringi, W. L. Randeu, and M. Schönhuber, "Drop shapes, model comparisons, and calculations of polarimetric radar parameters in rain," *J. Atmos. Oceanic Technol.*, vol. 24, pp. 1019–1032, 2007.

[31] M. I. Mishchenko and L. D. Travis, "Capabilities and limitations of a current FORTRAN implementation of the T-matrix method for randomly oriented, rotation symmetric scatterers," *J. Quan. Spec. Rad. Transfer*, vol. 60, pp. 309-324, 1998.

[32] C. Magono and T. Nakamura, "Aerodynamic studies of falling snowflakes," J. *Meteorol. Soc. Jpn*., vol. 43, pp. 139–147, 1965.

[33] G.M. Heymsfield et al., "The EDOP radar system on the high-altitude NASA ER-2 aircraft," *J Atmos Oceanic Tech*., vol. 13, pp. 795–809, 1996.

[34] L. Li et al., "The NASA High-altitude Imaging Wind and Rain Airborne Profiler," *IEEE Trans on Geosci and Rem Sens.*, vol. 54, pp. 298–310, 2016.

[35] L. Li et al., "A 94-GHz cloud radar system on a NASA high-altitude ER-2 aircraft," *J Atmos Ocean Technol*., vol. 21, pp. 1378–1388, 2004.

[36] M.L.W McLinden et al., "The NASA GSFC 94-GHz Airborne Solid-State Cloud Radar System (CRS)," *J Atmos Ocean Tech*. vol. 38, pp. 1001–1017, 2021.

[37] L. A. McMurdie, G. Heymsfield, J. E. Yorks, and S. A. Braun, "Investigation of Microphysics and Precipitation for Atlantic Coast-Threatening Snowstorms (IMPACTS): HIWRAP Data Collection," NASA EOSDIS Global Hydrometeorology Resource Center Distributed Active Archive Center, Huntsville, AL, USA, 2019. [Online]. Available: https://doi.org/10.5067/IMPACTS/HIWRAP/DATA101.

[38] R. Meneghini and H. Kumagai, "Characteristics of the Vertical Profiles of Dual-Frequency, Dual-Polarization Radar Data in Stratiform Rain," *J. Atmos. Oceanic Technol.*, vol. 11, pp. 701–711, 1994.

[39] V. N. Bringi, K. Vijay, and M. Thurai, 2023: *Advances in Weather Radar. Volume 1: Precipitation sensing platforms*. ISBN: 9781839536229, 542 pp. https://doi.org/10.1049/SBRA557F.